npj | urban sustainability

Article

Published in partnership with RMIT University

https://doi.org/10.1038/s42949-025-00288-8

# Local damages drive network-wide costs in compound flood-prone coastal city



Raviraj Dave[1], Sushobhan Sen[1], Avijit Maji[2] & Udit Bhatia[1,3]

Concurrency of extreme rainfall, river surges, and elevated tides can produce compound floods that single- or multi-hazard summation models frequently misrepresent flood extent and depth-particularly in the Global South, where rapid urban expansion intensifies infrastructure stress. Here, we show that, although summation-based approaches and a fully coupled hydrodynamic model yield comparable direct (infrastructure) damage estimates, the summation-based approach produces indirect (user) costs up to 40% higher than the compound model. By integrating compound flood modeling with microscale traffic simulations in Kozhikode, India, we find that neighborhoods with minimal inundation can nonetheless face severe gridlock and up to tenfold increases in vehicular emissions, underscoring how local flooding ripples throughout the city. This discrepancy in indirect costs risks substantial misallocation of limited resources and underscores the broader socio-economic burdens often overlooked by conventional flood risk frameworks. By capturing these correlated hazards and real-time road closures, we highlight the need for multihazard flood governance that effectively addresses both localized inundation and network-wide disruptions in rapidly urbanizing coastal cities.

Coastal cities across the globe, particularly those experiencing rapid urban growth in the Global South, must increasingly contend with multiple overlapping flood drivers: intense rainfall, riverine overflow, and tidal surges[1–3]. When these hazards coincide in close succession or occur simultaneously, compound flooding generates interactions that are not reliably represented by a simple summation of isolated events[4–6]. Recent large-scale floods in Southeast Asia, West Africa, Europe, and parts of the United States illustrate this escalating risk, as persistent rainfall merges with elevated coastal waters or upstream inflows to cause prolonged, city-wide disruption[7–10]. However, many existing flood risk models still treat each hazard driver independently, potentially underestimating the real extent of damage in densely urbanized areas[11–13].

Infrastructure disruptions in coastal urban corridors often reverberate beyond the immediate flood zone. Submerged roads, compromised drainage systems, and stalled transport routes can cripple economic activities and undermine public services[14–17]. Although these direct (or agency costs), such as repairing roads, have traditionally guided resource allocation[18–21], indirect (or user costs), including rerouting delays, traffic congestion, and greenhouse gas emissions, can be equally or even more significant[22–24]. Throughout this manuscript, the terms direct and agency costs are used interchangeably, as are indirect and user costs. For example, if an arterial highway floods during high tide, neighborhoods (commonly referred to as wards in India) that remain physically unflooded can still face hours of gridlock and business disruptions. However, standard assessments often overlook these indirect impacts, especially under overlapping flood drivers that prolong submersion or force repeated closure of critical corridors[11–13]. Addressing these gaps requires coupled modeling, in which pluvial (rainfall-driven), fluvial (riverine), and coastal (tidal) processes interact within an integrated hydrodynamic and mobility framework[25–27]. This integration is technically demanding, requires multiscale data, detailed boundary conditions, and robust computational methods, and remains relatively uncommon in operational planning contexts[28,29]. However, coupling reveals how high tides can impede river discharge, how extreme rainfall can overwhelm stormwater capacity, and how backwater effects can spread inland, leading to flood conditions that differ substantially from the sum of individual hazards[5].

Despite increasing recognition of compound flood dynamics, many established risk assessments still treat each hazard driver independently -an approach that typically underestimates impacts- or combine them via a simple summation. However, the reliability of such composite approaches remains uncertain, raising the possibility that they may either under- or overestimate disruption compared to fully coupled compound models.[22,30,31]. In densely built urban environments, even minor flooding can cause widespread disruptions in transportation networks, submerged roads, and compromised critical infrastructure[14–17]. These disruptions reverberate far beyond inundation zones, stalling public services and hindering

[1]Department of Civil Engineering, Indian Institute of Technology Gandhinagar, Palaj, Gandhinagar, Gujarat, India. [2]Department of Civil Engineering, Indian Institute of Technology Bombay, Powai, Mumbai, Maharashtra, India. [3]Department of Computer Science and Engineering, Indian Institute of Technology Gandhinagar, Palaj, Gandhinagar, Gujarat, India. e-mail: bhatia.u@iitgn.ac.in

economic activities[32,33]. In addition, conventional flood models typically focus on agency costs such as repairs to roads or bridges[18–21] - while overlooking user cost, including prolonged congestion, rerouting, supply chain delays, and elevated emissions[22–24,34–36].

Kozhikode, a coastal city in Kerala situated in southwestern India, exemplifies these intertwined challenges. Flanked by the Arabian Sea and the Kallai River and lying near the Western Ghats, it is often referred to as a gateway to the Indian summer monsoon, experiencing prolonged rainy seasons and frequent intense downpours. In addition, tidal inflows from the coast intersect with the city's undulating terrain, creating multiple pathways for water to accumulate or flow inland. The 2018 floods in the Kozhikode district affected more than 50,000 homes[37], yet local flood assessments often rely on simplified single-hazard models that underestimate tidal backflow and fail to capture inland "hot spots"[38,39]. Although a well-connected drainage system can mitigate pluvial flooding under normal conditions, high tides or elevated river levels can impede outfalls, overwhelming portions of the network and compounding localized inundation. Furthermore, direct cost estimates typically omit the dynamic impacts of rerouted traffic and increased vehicular emissions, overlooking broader socioeconomic consequences when critical roads are flooded-a problem that generalizes to many urban coastal cities in the Global South that face compound inundation[19,21].

In this study, we evaluate how local-scale damages translate into network-wide costs in a flood-prone coastal city. We develop independent, composite (linear summation of drivers), and compound (fully coupled interaction of drivers) flood scenarios through hydrodynamic simulations, and quantify both direct costs (infrastructure repair and maintenance) and indirect costs (travel delays, rerouting, and vehicular emissions) by dynamically coupling flood outputs with a microscale traffic model. By comparing composite and compound approaches, we examine disparities in estimated impacts and assess the large-scale disruption costs that can arise from locally induced floods. To achieve these objectives, we employ a fully coupled 1D-2D hydrodynamic model (MIKE+)[40] to simulate flood scenarios for Kozhikode under varying return periods, integrating pluvial, fluvial, and coastal processes. Direct infrastructure damage is estimated using depth-damage functions, while hourly flood outputs are integrated with a microscale traffic model (Simulation of Urban MObility - SUMO)[41], calibrated against open source Google Maps data[42], to capture real-time road closures triggered by inundation depths greater than 0.3 m[43]. We address these aims within a single framework because hazard dynamics and their cascading economic impacts are inseparably linked. Compound flooding not only intensifies local damages to infrastructure but also amplifies the secondary effects felt across the wider urban network, such as mobility disruptions, congestion, and emissions. Treating these components in isolation would obscure how localized flood damages reverberate through city-wide systems, whereas analyzing them together allows for a more comprehensive and policy-relevant understanding of flood impacts.

Our results show that while direct flood-related losses differ by only 1–2% between a compound model and naive summations of isolated hazards, indirect costs can diverge by up to 40%. This discrepancy poses critical policy challenges. On the one hand, relying solely on direct damage estimates risks underestimating the broader, city-wide disruption from compound flooding-particularly in emerging urban centers with limited resources and rapidly expanding road networks. Ignoring congestion impacts and emissions not only misrepresents the true socio-economic burden but may also lead to suboptimal resource allocation, such as prioritizing levees or seawalls over traffic management strategies and adaptive infrastructure upgrades. On the other hand, overestimating direct damages by aggregating separate hazard scenarios can prompt decision-makers to over-fund certain defenses at the expense of more balanced, network-focused interventions. Moreover, wards (equivalent to neighborhoods) that experience zero inundation can still incur significant user costs due to prolonged traffic congestion and associated emissions, highlighting how spatially concentrated flood events reverberate across an entire urban system.

## Results

We analyze how coastal, fluvial, and pluvial flood events - along with their compound interactions -affect an urban road network by incorporating local urban-scale processes (Fig. 1a). The study categorizes the impacts on the road network into three key areas: direct costs borne by the transportation agency, such as expenses for road repair and maintenance; indirect costs faced by road users, including delays caused by flood-induced congestion; and environmental impacts, specifically emissions related to greenhouse gas and air pollutants (vehicular emission) (Figs. 1c, d, 2). We use the 2018 extreme flood event as a baseline scenario, which had a devastating impact on the study region Fig. 3.

The spatial distribution of the 100-year compound flood hazard (*Methods* for calculation of 100-year magnitudes) (Fig. 4a) highlights how extreme precipitation, river overflow, and tidal surges converge to shape the Kozhikode flood. In inland neighborhoods, flooding is mainly due to clogged stormwater drains when intense rainfall exceeds capacity. In contrast, near the coast and downstream floodplain zones, elevated tide levels and river outflow raise water levels at drainage outfalls, inducing a backwater effect that pushes floodwaters inland. Most inundation under compound conditions remains between 0.3 m and 1.2 m deep, underscoring the interplay between pluvial-driven surges and coastal or fluvial influences. The baseline and 50-year flood maps are shown in (Fig. S4).

Focusing on single-driver floods provides additional insight. Coastal flooding (Fig. 4b) extends beyond the immediate shoreline, propelled upstream by tidal backwater, with depths of 1.2–3 m where ocean water meets river discharge. Fluvial flooding (Fig. 4c) concentrates along the Kallai River corridor, featuring similarly deep waters of 1.2–3 m but over a smaller floodplain. In contrast, pluvial flooding (Fig. 4d) proves more extensive, covering 20.71 $km^2$, compared to 1.95 $km^2$ (fluvial) and 1.36 $km^2$ (coastal). Despite its broad footprint, pluvial inundation is often shallower (below 1.2 m), indicating that extreme rainfall produces widespread surface flooding without necessarily resulting in deeper water levels seen in coastal or fluvial scenarios.

### Temporal variation of flood drivers

The time series shown in (Fig. 4e–g) capture the evolution of each flood driver across a 72-hour window, spanning baseline to 100-year return periods. In the coastal case (Fig. 4e), flood volumes align closely with the tidal peaks, reflecting the cyclical nature of ocean tides. Fluvial flood volumes (Fig. 4f) peak at 2.65–3.25 million $m^3$ during maximum upstream discharge, then decrease as the flow subsides, spanning from the baseline scenario to the 100-year return period. In contrast, the pluvial flood volume (Fig. 4g accumulates gradually during heavy rainfall, culminating in maximum volumes of 8.5, 12.75, and 17.65 million $m^3$ for baseline, 50-year, and 100-year intensities, respectively. Together, these spatial and temporal dynamics confirm that pluvial flooding dominates the total inundation area, whereas coastal and fluvial scenarios produce locally deeper water levels. Under compound conditions, backwater effects and concurrent peaks can further intensify flood severity, particularly near drainage outfalls and river confluence zones, with peak flood volumes of 10.34, 15.85, and 19.66 million $m^3$ (Fig. 4h). Whereas in the case of composite flooding, cumulative flood reaches to peak value of 11.16, 15.72, and 20.52 million $m^3$ (Fig. 4i), leading to overestimation of flood volume.

### Road inundation and direct damage: agency costs

The overlay of maximum flood inundation maps on the city road network (Fig. 5a) reveals varying degrees of disruption in different hazard scenarios for a 100-year return period. Coastal flooding alone submerges 19 road sections (1% of the network), while fluvial flooding affects 74 road sections (3%). Pluvial flooding is far more extensive, inundating 1215 road sections (50.39% of the total). When hazards coincide, compound flooding submerges 1239 road sections (51.38%), slightly exceeding the pluvial total. By comparison, the linear summation of all hazard drivers inundates 1,243 road sections (51.56%) marginally overestimating the number of road

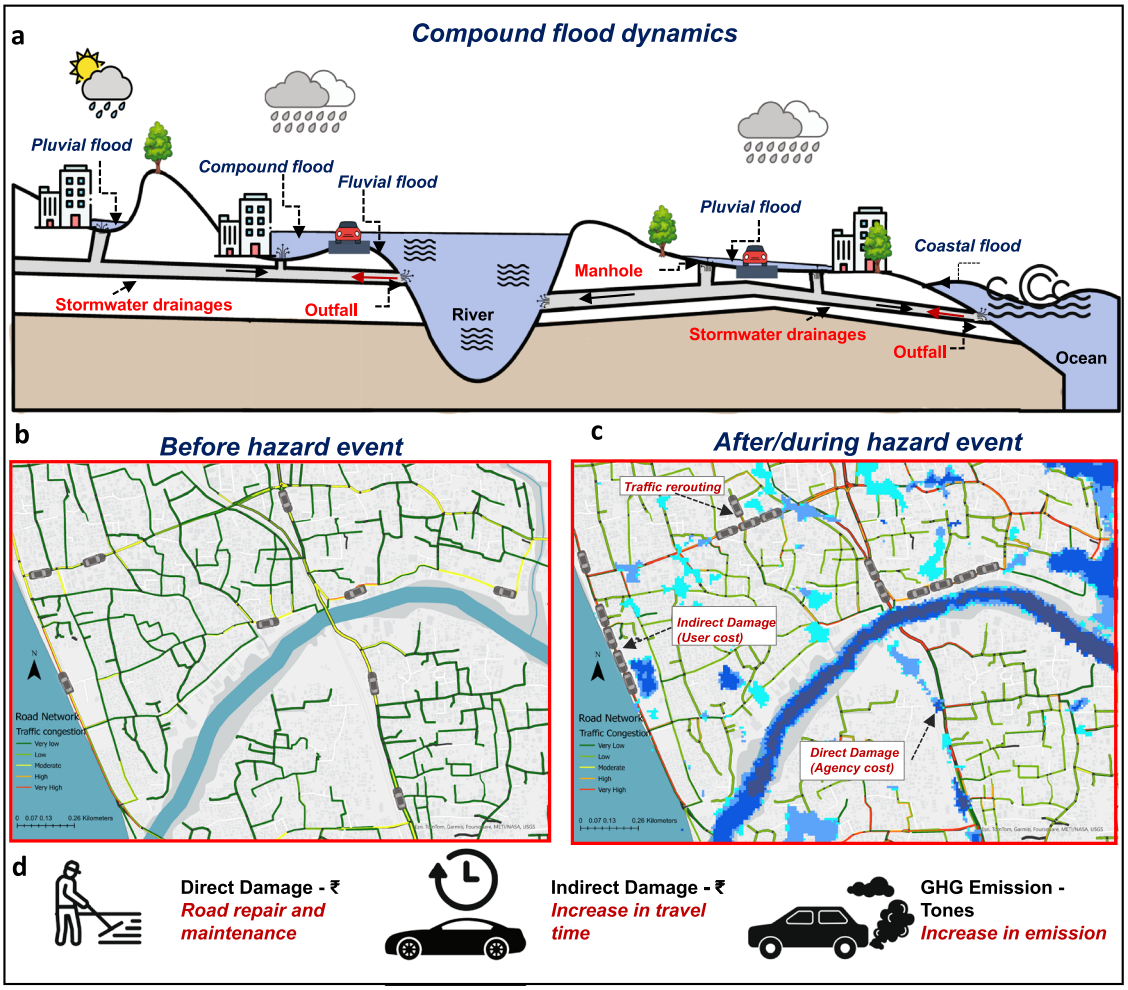


**Fig. 1 | Illustration of key compound flooding concept and associated roadway costs. a** Cross-section of a coastal region illustrating roads, residential areas, green spaces, an open coastline, a river cutting through the area, and an underground stormwater drainage system comprising pipes, manholes, and outfalls. The outfalls connect to both the river and the ocean, highlighting the intricate interplay of natural and built environments. Black arrows within the stormwater drainage indicate gravitational water flow direction, while a red arrow represents the backwater effect caused by reverse flow from the river and tides. Areas submerged due to extreme precipitation depict pluvial flooding, regions near the coast experiencing high tides illustrate coastal flooding, and river floodplain areas with high water levels show fluvial flooding. Zones where these processes converge are marked as experiencing compound flooding. **b** Conceptual illustration of vehicle movement showing normal traffic behavior prior to a flood event. **c** Depicts flood-induced roadway costs, including direct road damage and indirect damage from traffic congestion, resulting in time loss and increased vehicular emissions due to prolonged congestion. **d** Illustrates the types of flood-related road damage and their respective measurement units.

sections affected relative to the compound scenario. Tracking road inundation over a 72-hour period at the 100-year return level (Fig. 5b shows that coastal events exhibit tidal oscillations, while fluvial peaks coincide with maximum river discharge. Pluvial flooding initially increases sharply and then stabilizes, reflecting the intensity and duration of the rain. The compound scenario largely mirrors pluvial patterns, although tidal or fluvial interactions can prolong the flooding on key routes. The composite scenario exhibits a similar temporal pattern but with slightly higher peak values in terms of inundated roads.

Next, we evaluate direct costs (agency) in both spatial terms (Fig. 5c) and in aggregate across the study region (Fig. 5d). Coastal flooding imposes the highest ward-level costs (₹1.34 million [US$16k]) near shorelines, whereas fluvial flooding reaches ₹3.7 million [US$42.5k] around the Kallai river floodplain. Pluvial flooding, by contrast, causes a broader range of ward-level costs (₹1.8–39.2 million [US$20.6k–$450k]). Under compound conditions, costs reach ₹42.3 million [US$485.3k], extending into both low-lying coastal neighborhoods and inland neighborhoods prone to backwater effects. When direct costs are quantified using the linear summation of all drivers, the maximum ward-level cost reaches ₹ 39.1 million [US$485.3k]. At the city scale, this approach yields an overall direct cost that is higher by ₹ 0.6 million [US$7.8k] compared to compound flood scenario. The direct costs for baseline and 50-year return period events under isolated and compound flooding scenarios are provided in (Fig. S5).

Citywide (Fig. 5d), 100-year pluvial flooding (₹293.8–558.7 million [US$3.3–6.4 million]) vastly exceeds direct cost of fluvial (₹14.2–25.1 million [US$162.9–287.9k]) and coastal (₹1.2–2.3 million [US$13.7–26.4k]) combined. Compound flooding (₹306.4–575.2 million [US$3.51–6.59 million]) slightly surpasses pure pluvial levels, signaling that hazard concurrency can enhance damages. A naive linear summation of each scenario inflates overall agency costs by ₹3–11 million (US$34.4–126.2k), highlighting the need to model concurrency accurately.

## Flood induced traffic disruption and emissions

Flood-induced road closures generate indirect losses via congestion, increased travel time, and elevated emissions (Fig. 6). Coastal and fluvial floods usually reinforce typical rush-hour peaks with elevated travel time than typical hourly traffic, whereas pluvial and compound events spread heavy congestion throughout the day. At the 100-year level, pluvial flooding

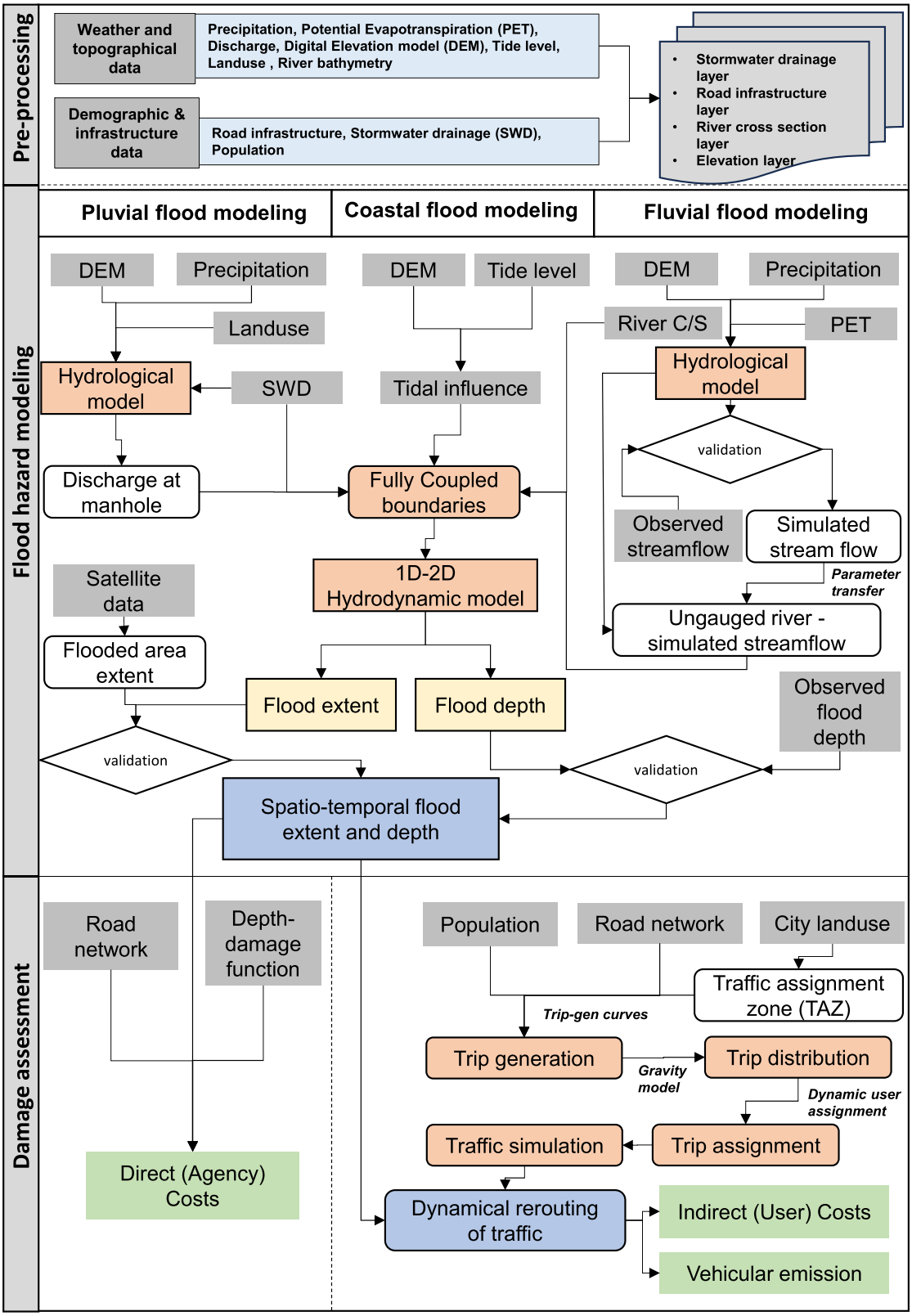


**Fig. 2 | Methodological flowchart.** Illustrating the inputs and outputs of the flood hazard and traffic simulation models used in this study. Isolated and compound flood hazards are integrated with depth-damage functions and traffic simulations to estimate direct (agency) costs, indirect (user) costs, and vehicle emissions resulting from flooding.

amplifies peak travel delays by a factor of 5.61 relative to baseline; compound events push it to 6.42 (Fig. 6f–h). A spatial breakdown of user costs (Fig. 6a–e) reveals distinct patterns across flood types. Localized coastal and fluvial floods tend to concentrate user costs around the directly submerged corridors, whereas pluvial flooding generates broader congestion hotspots across the network. Under pluvial scenarios, user costs peak at ₹2.24 million (US$25.7k). Compound flooding further amplifies these effects, with nearly all neighborhoods incurring positive net costs, sometimes reaching ₹2.21

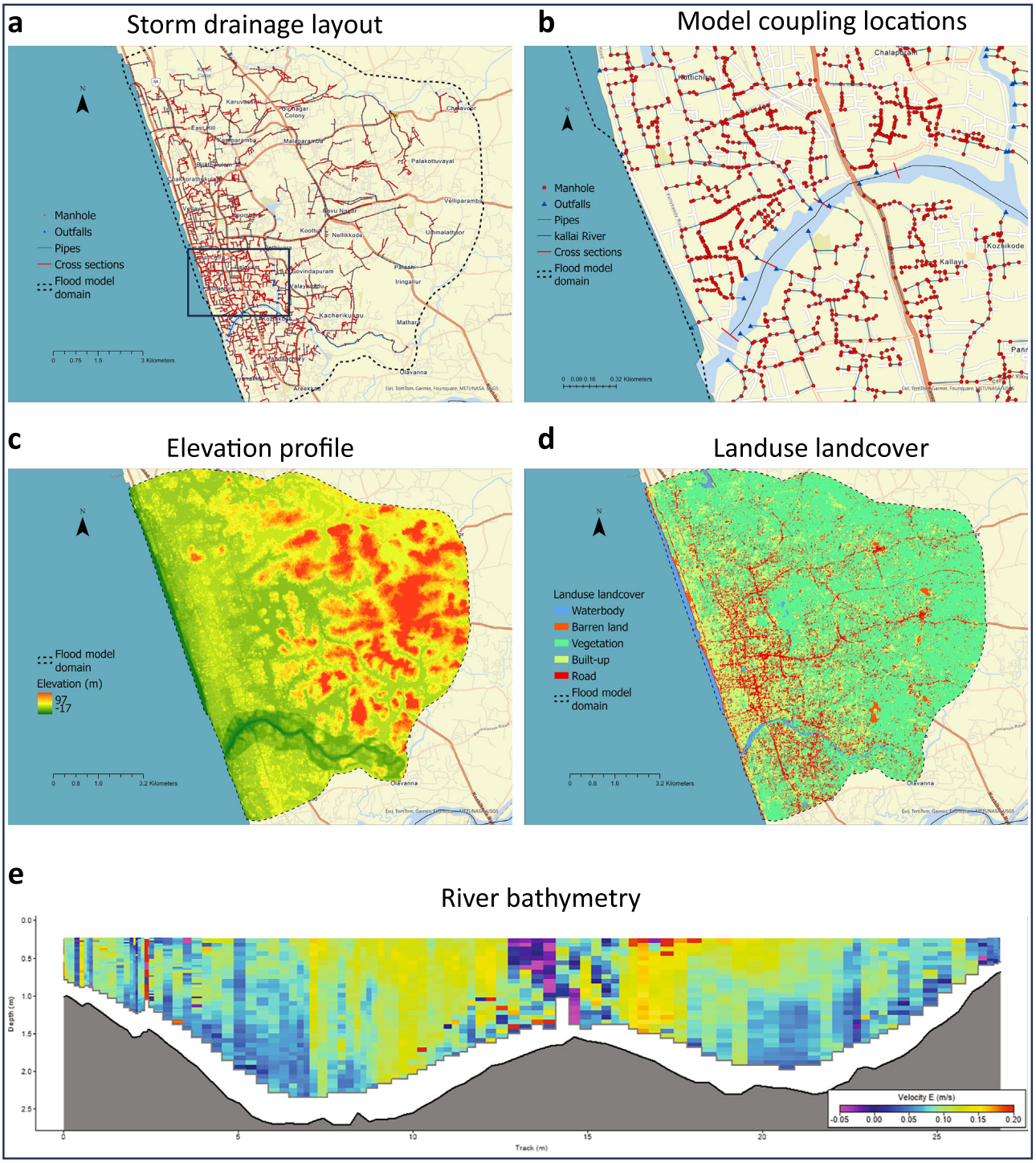


**Fig. 3 | Study area and supporting data sources. a** Stormwater drainage layout showing manholes, pipes, outfalls, and river cross-sections. **b** Zoomed-in view of the coupling location between the stormwater drainage outlet, river, and coastal boundary. **c** Elevation profile of the study domain. **d** Land Use Land Cover (LULC) classification derived from satellite imagery. **e** River bathymetry profile at a representative cross-section, measured using an Acoustic Doppler Current Profiler (ADCP).

million [US$25.3k]. In the case of linear summation of flood drivers, ward-level indirect costs increase further, reaching ₹4.23 million [US$48.4k] and thereby substantially overestimating impacts relative to the compound scenario. The net user cost under isolated and compound flood scenarios for the baseline and 50-year return period is presented in (Fig. S7). Rising congestion likewise drives vehicular emissions (Fig. 6i), where compound flooding can exceed normal traffic levels by over 1,000%. Linear summation again overestimates these emissions by 30–35% compared to compound flood scenario. Summarizing city-wide user costs (Fig. 6j) reinforces that pluvial flooding dominates these indirect costs, with compound scenarios slightly higher but still below naive additive sums. However, for the 100-year event, the composite scenario (linear summation of flood drivers) results in user costs that are 41.7% higher than those from the compound scenario. This indicates that ignoring coupled interactions among flood drivers can

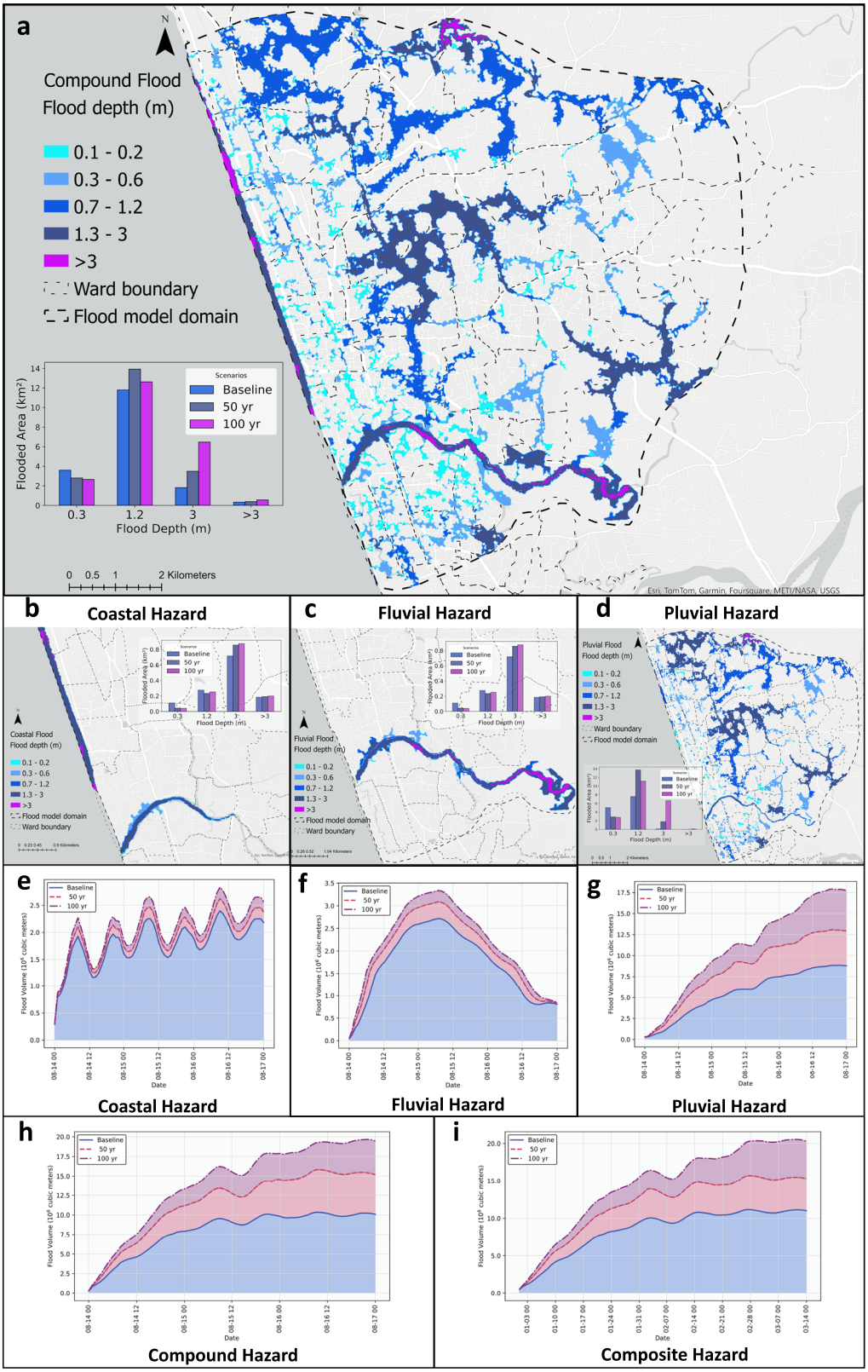


**Fig. 4 | Spatio-temporal pattern of flood inundation. a** Spatial distribution of the 100-year compound flood hazard, showing inundation extent and depth, with an inset bar graph illustrating the flooded area by depth. **b–d** Hazard exposure for coastal, fluvial, and pluvial floods. **e** Temporal flood volume for coastal scenarios: baseline, 50-year, and 100-year return periods. **f–i** Corresponding flood volume time series for fluvial, pluvial, compound, and composite scenarios.

substantially inflate cost estimates. This indicates that the composite model produces higher user costs than the compound model, underscoring that summation-based approaches can distort disruption estimates and should not be assumed to provide conservative or reliable benchmarks.

### Ward-level disparities between direct and indirect costs

Visualizing average direct (agency) and indirect (user) costs at the ward level for the 100-year return period (Fig. 7a–d) reveals further nuances. Under coastal and fluvial floods (Fig. 7a, b), some neighborhoods incur zero direct

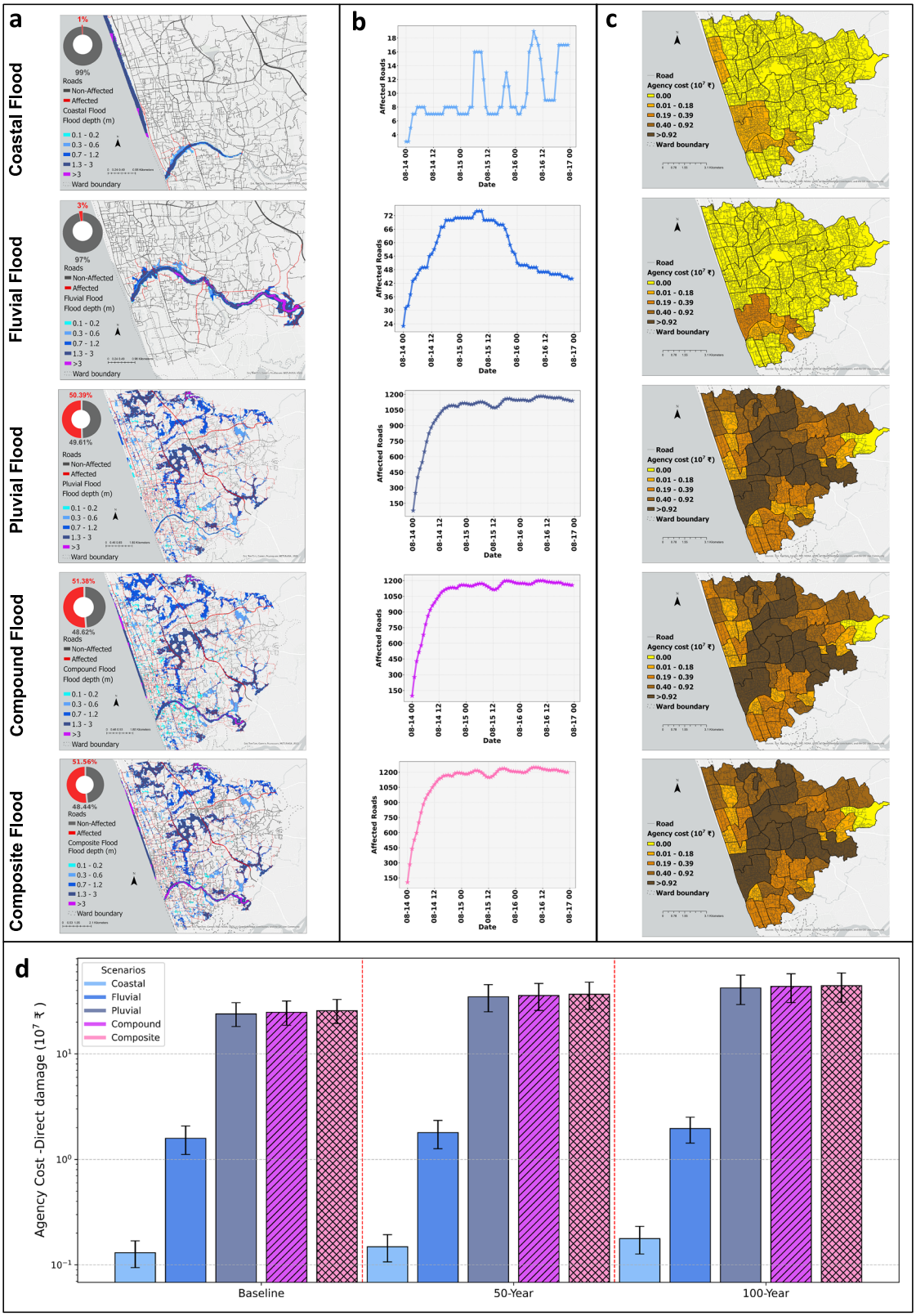


**Fig. 5 | Road perturbation and agency cost. a** Road inundation under coastal, fluvial, pluvial, compound, and composite flood scenarios for a 100-year return period, with the inset pie chart illustrating the percentage of inundated roads under individual, compound, and composite scenarios. **b** Temporal evolution of road perturbation over 72 hours due to flood inundation, showing tidal-wave induced inundation (coastal), road impacts from river overflow (fluvial), stormwater drainage overflow during extreme precipitation (pluvial), and corresponding time series for compound and composite scenarios. **c** Ward-wise financial losses from direct flooding impacts on the road network, depicting the average agency cost of road repairs under coastal, fluvial, pluvial, compound, and composite flooding. The gradient from light to dark gold indicates the range of ward-level agency costs, from lowest to highest. **d** Overall agency cost estimates across the study region for baseline, 50-year, and 100-year return periods under coastal, fluvial, pluvial, and compound flood scenarios. The composite scenario represents a linear combination of coastal, pluvial, and fluvial flood scenarios. Uncertainty bounds reflect variations in monetary values based on flood depth-to-damage relationships.

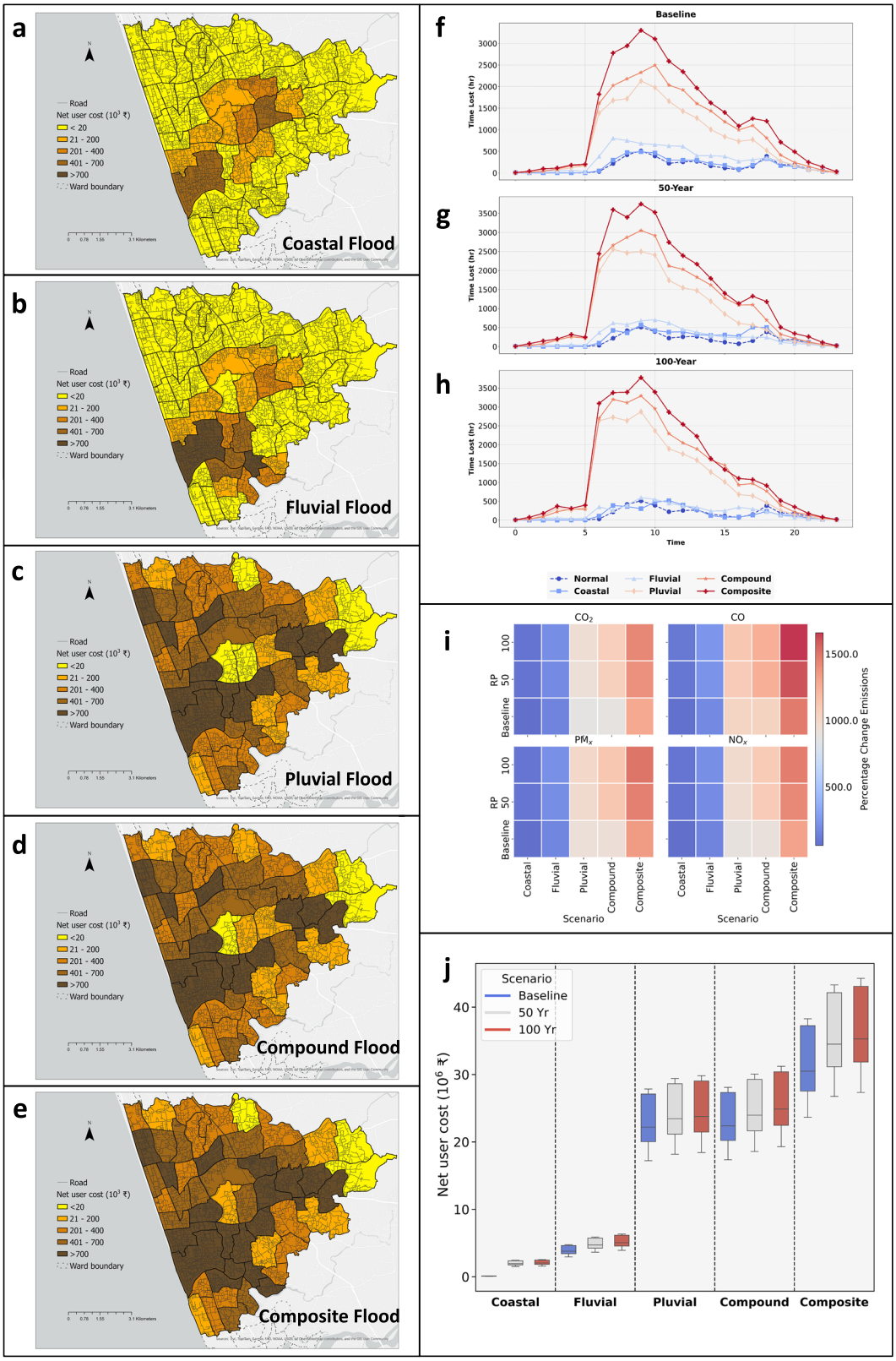


**Fig. 6 | Spatio-temporal characteristics of flood induced traffic. a–e** Spatial distribution of financial costs associated with travel time loss in an inundated road network for coastal, pluvial, fluvial, compound and composite floods. The gradient from light to dark gold represents the range of average net user costs incurred by neighborhoods, from lowest to highest. **f** Temporal behavior of road traffic under the baseline scenario (2018), illustrating time lost (in hours) due to traffic congestion across normal, coastal, fluvial, pluvial, compound and composite flood scenarios. **g**, **h** Temporal evolution of time loss for 50-year and 100-year return period scenarios, respectively. **i** Heat map showing the percentage change in vehicular emission from normal conditions to coastal, fluvial, pluvial, compound, and composite flood scenarios. **j** Estimation of net user costs for coastal, fluvial, pluvial, compound, and composite flood scenarios, with colors indicating baseline, 50-year, and 100-year return periods. Uncertainty ranges reflect variations in travel time value across income groups and trip distances.

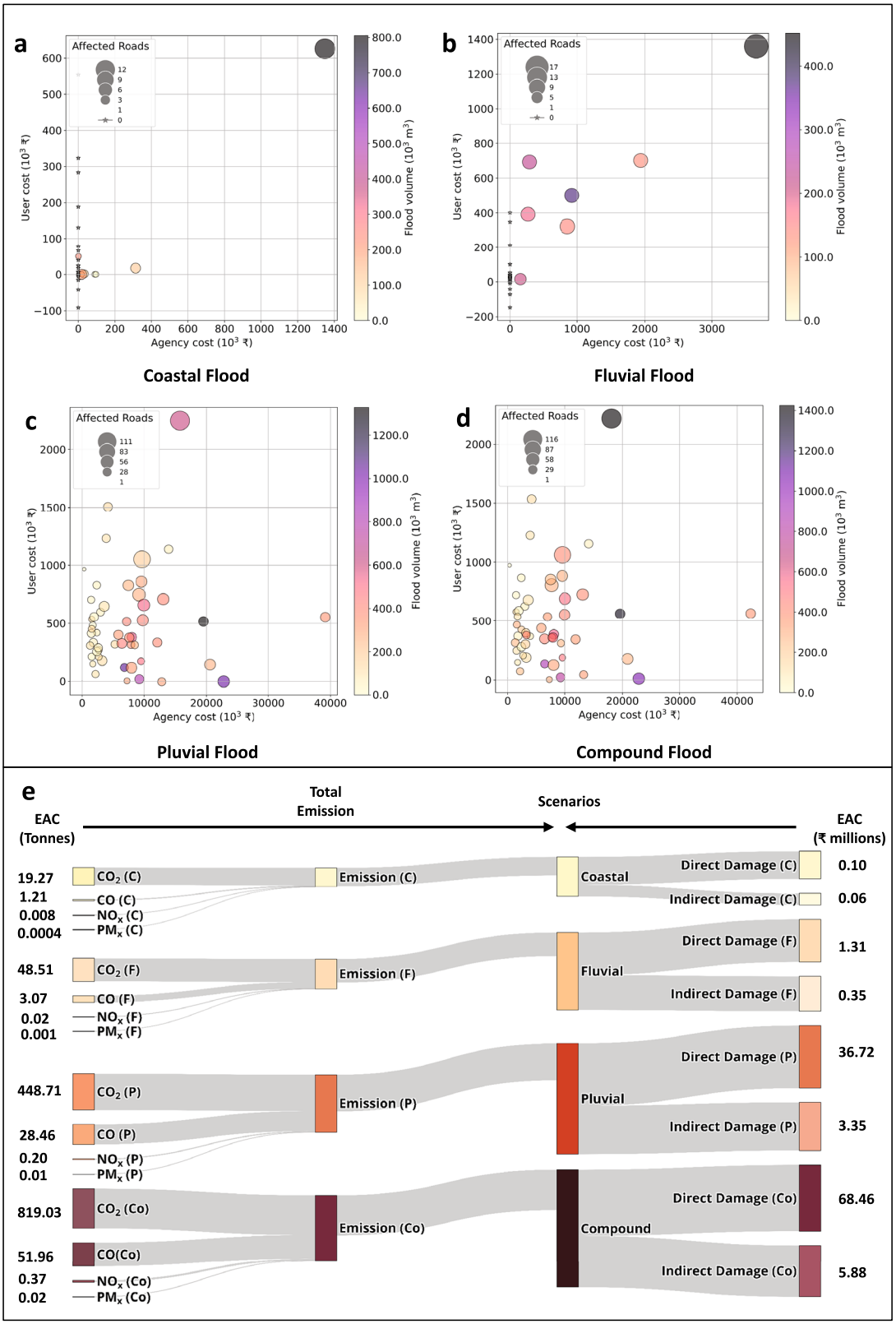


**Fig. 7 | Agency cost vs user cost and expected annual cost. a–d** Bubble charts illustrating the relationship between average agency costs (direct damages) and average user costs (indirect damages) for each ward. The x-axis represents agency costs, while the y-axis shows user costs. Bubble size corresponds to the extent of inundated roads, and bubble color reflects the flood volume within the ward. **a** Highlights user and agency costs for each ward due to coastal flooding, with star-marked bubbles indicating neighborhoods with zero agency costs but varying user costs. **b–d** Display the costs incurred by neighborhoods from fluvial, pluvial, and compound flooding, respectively, showcasing the disparity between user and agency costs across different neighborhoods. **e** Expected annual cost from coastal, fluvial, pluvial, and compound flooding, categorized into direct damage (agency cost) and indirect damage (user cost). Additionally, it presents the expected annual vehicular emissions associated with each flood driver, segmented into $CO_2$, CO, $NO_x$, and $PM_x$.

(agency) costs but substantial indirect (user) costs, underscoring the reach of rerouting and congestion beyond actual flood zones. Pluvial flooding (Fig. 7c) breaks any straightforward link between flood volume and costs: neighborhoods with fewer flooded roads can still face high direct losses, while heavy-inundated neighborhoods exhibit reduced indirect costs if drivers avoid them. Compound flooding (Fig. 7d) echoes these disproportionate patterns, where wards experiencing higher flood volumes typically face elevated user and agency costs. However, even neighborhoods with moderate flood volumes can incur significant user costs due to spillover congestion. While direct correlation between agency and user costs may sometimes exist (e.g., in coastal floods), in many cases (e.g., pluvial and compound floods), significant user costs occur independently of agency expenditures. This finding highlights the importance of comprehensive impact assessments that integrate both direct (infrastructure repair) and indirect (user disruption) costs, as neglecting either dimension can distort the true scale of flood impacts and compromise the effectiveness of resilience planning. The comparison of average costs and user costs for the baseline and 50-year return period is presented in (Fig. S8).

Finally, weighting the baseline, 50-year and 100-year events by their respective probabilities, we quantify the expected annual cost (EAC) (Fig. 7e). Compound flooding surpasses individual flood types by factors of 464.62, 44.78, and 1.85 when compared to coastal, fluvial, and pluvial scenarios, respectively. Emissions align with this trend: coastal floods produce roughly 20.48 t $CO_2$ annually, fluvial about 51.60 t, pluvial 477.38 t, and compound 871.38 t. These findings confirm that while pluvial events drive the most pervasive impacts, overlapping tidal and river influences in compound scenarios can further intensify socioeconomic losses and environmental burdens. Accounting for these concurrent flood dynamics is vital for prioritizing multihazard governance in fast-growing coastal cities confronting intensifying climate extremes.

## Discussion

Compound flooding, arising from the concurrent interplay of pluvial, fluvial, and coastal processes, poses a significant challenge to rapidly growing coastal regions worldwide[44–46]. Although the concept of compound flooding is gaining broader recognition, many assessments still isolate each driver or simply sum their effects, neglecting the complex interactions-such as backwater dynamics and overlapping inundation zones-that can reshape overall impacts[11–13,22]. By integrating a fully coupled 1D-2D hydrodynamic model with dynamic microscale traffic simulations, our work demonstrates how concurrency among these hazards not only exacerbates direct costs but also triggers substantial indirect burdens, including elevated travel times and vehicular emissions.

One crucial finding is the prominent role of pluvial (rainfall-driven) flooding. At 50 and 100 years of return periods, extreme rainfall alone can encompass larger inundation footprints than either coastal or fluvial events. When rainfall coincides with river overflow or tidal surges, simple additive events overestimate losses compared to compound events. Importantly, while direct damages remain relatively comparable between summation-based and fully coupled approaches, indirect costs diverge substantially-by around 40%-since traffic disruptions, delays, and emissions are strongly shaped by nonlinear interactions between flood drivers. Notably, this also reveals that the composite (summation-based) models may overestimate user-related costs, as their additive treatment of flood drivers inflates inundation extent and duration, thereby exaggerating mobility disruptions even when physical damages remain comparable. Moreover, neighborhoods that appear unflooded can still face severe congestion and up to tenfold emission spikes during prolonged detours, revealing how local flood conditions propagate throughout an interconnected urban network and impose broader environmental tolls. Collectively, these findings emphasize the necessity of compound flood modeling and integrated cost assessments to more accurately capture cascading urban impacts and to inform effective resilience and adaptation strategies.

Although this study incorporates high-resolution bathymetric data, traffic information, and satellite imagery, several avenues could improve both resolution and scope. Real-time sensor networks and continuous river gauges would capture sub-daily fluctuations in rainfall and discharge, supporting more adaptive flood forecasting. Similarly, while we employed the best publicly available 10 m DEM[47] for terrain representation, LiDAR-derived DEMs at 1-2 m resolution would more accurately capture fine-scale urban topography, including small depressions and narrow streets, and could further refine flood extent simulations. However, higher spatial resolution alone does not address other key gaps in representing urban flood processes, such as the absence of detailed stormwater drainage networks in available datasets, which remain a critical source of uncertainty.

We did not incorporate progressive speed reductions below the 0.3 m closure threshold[14], which may slightly understate disruption in shallowly flooded streets; however, this simplification provides a conservative and widely used basis for safety-based closure decisions[43]. Our use of trip generation rates from the ITE Trip Generation Manual[48–50], rooted largely in North American contexts, may not fully reflect local conditions in Kozhikode or other Indian cities. By integrating land-use data from Kozhikode[51] and validating against publicly available Google Maps traffic data, we aim to bridge these discrepancies, but locally tailored trip generation models could improve accuracy, particularly for forecasting peak-hour congestion and vehicle miles traveled. In addition, we assumed that overall trip-making demand remains constant during flood events, with only trips whose origins or destinations were inundated being canceled. This simplification is consistent with empirical evidence from Indian cities, where many commuters continue traveling despite disruptions due to employment and essential needs[22,36,52–54]. Nonetheless, additional adaptive behaviors-such as voluntary trip suppression in nearby zones, altered departure times, or mode shifts-were not captured. Incorporating such behavioral responses into coupled flood-traffic models remains an important direction for future research and could further refine estimates of user costs. Due to the lack of detailed multimodal traffic data, only passenger car traffic was considered in this study. Passenger cars represent a large portion of urban traffic, and while including freight, public transport, and two-wheelers could further enrich the analysis, the percentage shifts observed are expected to remain largely representative of overall network trends. Despite these constraints, the approach remains largely applicable to the observed network behaviors. Our focus on passenger car traffic excludes public transit, freight, and broader social dimensions, suggesting that future work could pursue more comprehensive modeling that incorporates local conditions, multiple transport modes, and varying levels of infrastructure vulnerability.

While this study focuses on Kozhikode, India, the coupling framework we present is readily adaptable to coastal cities worldwide. The key aspects of the framework-including flood hazard modeling, road network impacts, and user cost calculations-are transferable to a variety of urban areas with diverse geographic and socio-economic conditions. Although Kozhikode is not a coastal megacity, the methodological approach is scalable and can be applied to cities of different sizes and complexities, whether mid-sized towns or large metropolitan regions exposed to compound flood risks. Collaborations with local authorities and periodic traffic counts would enrich the empirical basis for modeling, while enhanced sensor networks could provide real-time flood extents and traffic flows for adaptive congestion management. From a policy perspective, embedding this integrated approach in municipal or regional decisions could help guide stormwater infrastructure improvements, enact land use zoning that restricts development in high-risk floodplains, and develop proactive congestion mitigation strategies.

Our findings indicate that conventional barriers or levees alone may be insufficient if extreme rainfall coincides with other flood drivers and that roads outside inundation zones can nevertheless incur substantial indirect burdens. These findings emphasize the need for integrated strategies that address stormwater drainage upgrades, upstream retention, and cross-agency disaster coordination. In addition, soft and nature-based strategies

can complement these hard measures. Wetlands, green infrastructure, and improved stormwater management can reduce runoff and enhance local absorption capacity, while behavioral interventions such as early warning systems, real-time route-closure notifications, and work-from-home advisories can limit indirect user costs during extreme events. Although these measures were not explicitly modeled in this study, the coupled flood-traffic framework developed here provides a foundation for evaluating their effectiveness in future work. Overall, this work shows how flood impacts extend beyond obvious points of inundation, reshaping transportation networks and local economies in ways that additively derived models often misrepresent. As climate extremes intensify, adopting a multihazard framework - one that explicitly captures the interplay of rainfall, river discharge, and tidal surges - will be essential for safeguarding infrastructure and community resilience. This integrated perspective is particularly urgent for coastal regions in the global South, where infrastructure deficits and demographic pressures increase systemic risks[55]. Adopting data-driven and adaptive planning approaches can provide coastal cities with a pathway to resilience-mitigating both direct damages and hidden societal costs while fostering more equitable and enduring strategies for a flood-prone future.

## Methods

### Study area

We investigate the isolated and compound impacts of multiple flood drivers on the road infrastructure systems of the coastal city of Kozhikode, located in Kerala, India. The study domain encompasses the municipal corporation region of the city, which is part of the Kallai River catchment (Fig. S1). This complex urban area experiences the spatial convergence of flood-inducing factors such as extreme precipitation, riverine overflow, and tidal surges. The region features a highly undulating topography, with the eastern part of Kozhikode characterized by landforms such as beach ridges, sandbars, and backwater marshes. Moving a few kilometers inland, the terrain transitions into slopes and clustered hills interspersed with numerous valleys. The study area experienced an extreme precipitation event in August 2018, resulting in 16 fatalities and about 50,000 houses severely affected by floods[37].

### Flood hazard model

Flood hazard estimation was conducted using the MIKE+ software[40], which employs an implicit finite difference numerical scheme to solve the full shallow water equations[56]. The modeling process begins with the solution of the 1D shallow water equations to simulate flow in stormwater drainage and river channel flows. Subsequently, the model extends to solve the full 2D Saint-Venant equations, integrating the 1D and 2D flows for a comprehensive simulation. The governing equations include the continuity equation and two momentum equations, each representing flow dynamics in orthogonal directions.

$$\frac{\partial \mathbf{U}}{\partial t}+\frac{\partial \mathbf{F}(\mathbf{U})}{\partial x}+\frac{\partial \mathbf{G}(\mathbf{U})}{\partial y}=\mathbf{S}(\mathbf{U}) \tag{1}$$

where,

$$\mathbf{U}=\begin{bmatrix} h \\ hu \\ hv \end{bmatrix},\quad \mathbf{F}(\mathbf{U})=\begin{bmatrix} hu \\ hu^2+\frac{1}{2}gh^2 \\ huv \end{bmatrix},$$

$$\mathbf{G}(\mathbf{U})=\begin{bmatrix} hv \\ huv \\ hv^2+\frac{1}{2}gh^2 \end{bmatrix},\quad \mathbf{S}(\mathbf{U})=\begin{bmatrix} 0 \\ -gh\frac{\partial z}{\partial x}+S_x \\ -gh\frac{\partial z}{\partial y}+S_y \end{bmatrix}$$

where $U$ represents the state vector containing the conserved quantities, $F(U)$ and $G(U)$ are the flux vectors in the $x$ and $y$ directions, respectively. $S(U)$ is the source term vector accounting for bed slope and other forces.

To accurately represent the complex topography of Kozhikode city, high-resolution elevation data with a 10-meter spatial resolution from CartoDEM[47] provided by the National Remote Sensing Centre (NRSC) was utilized. Additionally, the National Centers for Environmental Information (NCEI) Coastal Elevation Model was employed to capture the ocean bathymetry near the coastal region[57]. For river bathymetry, Acoustic Doppler Current Profiler (ADCP)[58,59] and Real-Time Kinematic Differential Global Positioning System (RTK DGPS) devices were used to measure river depth and velocity across multiple cross-sections (Fig. 2e). The Digital Elevation Model (DEM) was further refined through hydroconditioning processes. Initially, CartoDEM and NCEI Coastal DEM elevations were merged at the coastline. Subsequently, the DEM was hydroconditioned within the river channel by adjusting elevations to align with river bathymetry data collected through in situ measurements (Fig. 2c). The hydrodynamic model was configured to ensure the most accurate and robust simulation outcomes. A triangular irregular network (TIN) mesh was generated to represent the terrain's topographical properties, with grid sizes ranging from a minimum of 1 $m^2$ to a maximum of 200 $m^2$ within the domain boundary. Furthermore, the Manning roughness coefficient was developed to model flow resistance based on the land use land cover (LULC) map derived from a combination of Sentinel-1 and Sentinel-2 10-meter raster grids. The methodology and accuracy of the LULC classification are detailed in (Note S1 and Fig. 2d). The MIKE+ model was set up to simulate the following hazard models.

The pluvial flood model was configured using precipitation inputs from ERA5-Land reanalysis for a 72-hour extreme rainfall event in 2018 at a spatial resolution of 0.1° and an hourly temporal scale[60]. The 50-year and 100-year design rainfall intensities were derived through flood frequency analysis using the Generalized Extreme Value (GEV) method, as detailed in (Note S2). In the pluvial flood scenario, infrastructure plays a crucial role in managing surface runoff. The model incorporated stormwater drainage data, including 6274 manholes, 6278 pipes, and 66 outfalls, to accurately represent the drainage network's capacity and flow dynamics (Fig. 2a, b). To simulate the isolated pluvial flood scenario, the river stage during the low-flow period was considered, with no tidal influence at the stormwater drainage outfalls. The flow in stormwater drainage is solved through the 1D-Saint Venant equation (Eq. (2)) and later coupled with 2D-overland flow solved by (Eq. (1)).

$$\begin{aligned} &\tfrac{\partial A}{\partial t}+\tfrac{\partial Q}{\partial x}=0 \\ &\tfrac{\partial Q}{\partial t}+\tfrac{\partial}{\partial x}\left(\tfrac{Q^2}{A}+gAh\right)=gA(S_0-S_f) \end{aligned} \tag{2}$$

where $A$ is the cross-sectional area of the flow, $Q$ is the flow discharge, $h$ depicts flow depth, $S_0$ and $S_f$ are bed and friction slope, respectively.

The fluvial flood scenario was configured by specifying the water source in the river stream. Due to the absence of a gauge station in the Kallai River catchment, the parameter regionalization with the donor catchment approach was employed[61] to simulate the hydrological model. The nearby Chaliyar River catchment, which shares similar topography and land-use characteristics, was modeled using the SIMHYD (Simple hydrology model), a conceptual rainfall-runoff model that simulates streamflow based on rainfall, evapotranspiration, and catchment characteristics[62,63]. The model was configured with precipitation data and GLEAM (Global Land Evaporation Amsterdam Model) potential evapotranspiration data[64]. The model was calibrated and validated against observed streamflow data from INDIAWRIS (India Water Resources Information System)[65], and the validated parameters were transferred to the un-gauged Kallai River catchment to estimate streamflow for the fluvial flood scenario (Fig. S2). A detailed explanation of the hydrological model is provided in (Note S1). The simulated streamflow was used as a boundary condition for the hydrodynamic model. The hydrological model was applied across the upstream catchment area of the Kallai river to capture runoff generation, while the hydrodynamic model encompassed the river channel and adjacent floodplains within the urban extent of the Kozhikode Municipal Corporation to simulate inundation dynamics. The 50-year and 100-year flow rates were estimated based on flood frequency analysis using the GEV method, as

detailed in (Note S2). In situ, river cross-sections were incorporated for 1D river channel flow to simulate the isolated fluvial flood scenario, which was then coupled with 2D overland flow (Fig. 2e). Flow contributions from stormwater drainage outfalls and tidal levels were not accounted for in this scenario.

The coastal flood scenario was developed using hourly tide level data from in-situ tidal sensors provided by the Indian National Centre for Ocean Information Services (INCOIS)[66]. The 50-year and 100-year tide levels were estimated using the peak-over-threshold method, as detailed in (Note S2). This scenario incorporates tide fluctuations through shallow water equations for an area extending a few kilometers from the coast. However, it does not account for additional coastal flood drivers such as wave transformation, runup, and overtopping[27]. The tide levels were incorporated into the hydrodynamic model as a 2D boundary condition, while the influence of stormwater drainage outfalls and upstream river inflows was excluded to create an isolated coastal flood scenario.

Each hazard scenario (pluvial, fluvial, and coastal) was fully integrated into the hydrodynamic model. The stormwater drainage outlets were connected to the river channel to couple the pluvial and fluvial floods, while outlets discharging into the ocean were linked to tide levels to account for coastal-pluvial flood interactions. Additionally, the downstream section of the river channel was coupled with the coastal boundary through tide levels, ensuring dynamic interaction between each hazard driver. The baseline, 50-year, and 100-year precipitation intensity, streamflow, and tide levels were used to generate the corresponding return period boundary conditions for compound flooding scenarios.

The hydrodynamic model representative of the compound flood scenario was validated using two complementary approaches. First, the 72-hour event from August 14 to August 17, 2018, was simulated by incorporating streamflow, precipitation, and tide levels to create a baseline scenario. The simulated flood depths showed an 80% match with observed depths at 104 points provided for Kozhikode Corporation by the Kozhikode corporation by the Kerala State Disaster Management Authority (KSDMA)[67,68]. Second, the model's flood inundation extent was validated using Sentinel-1-derived water body extents to ensure consistency with observed flood inundation patterns. This comparison yielded an overall accuracy of 0.77, an F1 score of 0.783, and a kappa coefficient of 0.419 when compared to satellite-derived flood maps. Here, overall accuracy represents the proportion of correctly classified flood and non-flood grid cells compared to the satellite-derived reference map (Note S3 and Fig. S3).

### Direct (agency) cost analysis

The impact of floods on roads was assessed by analyzing both direct and indirect damages. Road network data were sourced from OpenStreetMap (OSM)[69], which provided road width classifications based on OSM-defined categories such as highway, primary, secondary, tertiary, and residential roads. Direct economic damages were quantified using a depth-damage function database developed by ref. 70, which estimates flood-related losses on a national scale. These depth-damage functions range from 0 (no damage) to 1 (complete damage), reflecting the proportion of damage relative to flood depth. For this study, the maximum loss value and depth-damage functions specific to India were utilized, with road infrastructure considered as the primary exposure element. The depth-damage function was applied based on the flood inundation depth for each affected area.

Inflation adjustments were made using the Consumer Price Index (CPI) from the World Bank[71] to align financial loss estimates with current values, as the original database is based on 2010 price levels. The total direct financial loss, referred to as the agency cost, was calculated by summing the loss values across each raster grid (same as DEM) within the flood domain. This agency cost was computed for all flood inundation scenarios using Eq. (3).

$$\mathrm{C_A} = \sum_{i=1}^{n} D_{x(i)} \times f\left(d_i\right) \times A_i \tag{3}$$

where $C_A$ (agency cost) represents the total economic losses due to direct damage to the roads in the study area. The variable n denotes the total number of damaged road elements, $x(i)$ depicts the category of $i$th damaged road element, $D_{x(i)}$ is the maximum monetary damage for the i-th road element, $d_i$ represents the inundation depth of the i-th road element, and f symbolizes the proportion of the element destroyed. $A_i$ is the affected area of $i$th road element.

### Indirect (user) cost analysis

Road networks are also susceptible to indirect damage from floods, resulting in increased traffic congestion and heightened vehicular emissions. Traffic simulation models are commonly employed to evaluate the movement of traffic through a road network, which depends on user behavior, vehicle characteristics, traffic characteristics, etc.[23]. In this study, the Simulation of Urban MObility (SUMO)[41,72] was utilized to model the movement of vehicles in both spatial and temporal dimensions. SUMO is based on a gap-based car following model, in which vehicles dynamically adjust their speed to avoid collisions while still trying to reach their destination. The model is also capable of modeling typical user behavior, such as lane change and calculating data such as travel time and greenhouse gas emission, and air pollutants from each simulated vehicle. The road network data extracted from OpenStreetMap (OSM) was refined using JOSM (Java OpenStreetMap Editor) to ensure accuracy in street dimensions, permissible road speeds, and traffic control regulations. Road capacities were estimated from OSM road classifications, with representative values assigned to each class: trunk roads (four lanes, 80 km/h), primary roads (two lanes, 60 km/h), secondary roads (two lanes, 50 km/h), tertiary roads (two lanes, 40 km/h), and residential roads (single lane, 30 km/h). These values were derived from standard urban traffic engineering references and adjusted for Indian urban conditions where local data were unavailable[73–75]. For this study, it was assumed that all vehicles on the road were passenger cars.

Establishing baseline traffic conditions can be achieved in two ways: by using field traffic count data or through travel demand modeling. Since traffic count data were unavailable for the study area, as the local municipality does not collect this information, we developed a travel demand model instead. This model consists of trip generation, where we created origin-destination-based traffic demand models to map commuting patterns. Traffic Assignment Zones (TAZs) were delineated based on various land-use classifications within the study area, including residential, commercial, and other categories. Trip generation for each TAZ was estimated using guidelines from the ITE Trip Generation Manual[48], which provides detailed trip generation curves for estimating trip generation accounting for both peak and non-peak hour traffic. Since a local trip-generation manual is not available for Indian cities, trips were estimated using the ITE Trip Generation Manual in conjunction with local land-use characteristics. The resulting OD matrix included primarily home-based trips (work, school, recreation) along with a smaller share of pass-by trips, thereby covering all trip purposes defined in the Manual. Once trip generation was completed, trips were distributed among the TAZs using the gravity model (Eq. (4)).

$$T_{ij} = \frac{O_i \cdot D_j}{C_{ij}^{\beta}} \tag{4}$$

where $T_{ij}$ represents the number of trips between origin $i$ and destination $j$, $O_i$ is the trip production at origin $i$, and $D_j$ is trip attraction at destination $j$. the term $C_{ij}$ denotes the travel cost, typically based on the distance between origin $i$ and destination $j$. The parameter $\beta$ captures the sensitivity of trips to travel distance.

The gravity model generates the Origin-Destination (OD) matrix, which is subsequently utilized by the Dynamic User Equilibrium (DUE) model within SUMO to assign routes to individual vehicles based on real-

time conditions and driver behavior. Unlike static assignment, where routes are predetermined, DUE dynamically adjusts vehicle paths in response to evolving traffic conditions[76]. This model considers factors such as congestion, travel time, and road capacity to continuously refine vehicle routes during the simulation, leading to more realistic representations of driver behavior. The process iterates until an equilibrium state is reached, where no vehicle can significantly reduce its travel time. Finally, the traffic simulation is executed using the routes established by the DUE model. The travel time loss and air quality impacts due to transportation were assessed, and a baseline scenario for the traffic model was generated for 72 hours, matching the duration of the flood event. To convert travel time losses into monetary terms, we multiply the time loss observed in the model by the value of travel time in Kozhikode, as characterized by income groups and trip distances[77]. This calculation yields the user cost associated with traffic congestion. To quantify vehicular emissions, we used HBEFA v4.2 (Handbook of Emission Factors for Road Transport) to calculate fuel consumption and emissions per vehicle based on vehicle movement. HBEFA provides emission factors for various vehicle categories under different traffic conditions[78].

In the absence of real-time traffic counts, conventional methods for traffic model validation were not feasible. As an alternative, the traffic model was validated using Google Traffic Maps by visually comparing simulated traffic with typical observed congestion conditions at various locations. Additionally, 2500 stratified random sampling points were generated across the road network in the study area, and traffic speeds at these points were compared with corresponding speeds from Google Maps. The validation yielded an overall accuracy of 0.85, with a weighted F1 score of 0.854 and a kappa coefficient of 0.339, demonstrating a high level of agreement between the simulated and observed traffic conditions (Note S4 and Fig. S6).

The flood hazard data was dynamically integrated with the traffic model to accurately simulate traffic behavior during flooding events. Hourly flood propagation data were extracted from the flood hazard model for both isolated and compound flood events and then incorporated into the traffic model through rerouters, which reassign vehicles to different routes whenever a road becomes unavailable. The microsimulation assumes the same Origin-Destination (OD) matrix as the baseline scenario, without considering demand reduction during flooding. This approach isolates the impact of road network disruptions on travel delays and user costs, under the assumption that trip-making behavior remains constant during flooding events. Since OpenStreetMap (OSM) does not provide elevation data for the road network, we assigned ground surface elevation from the Digital Elevation Model (DEM) to the roads. For sections identified as bridges or overpasses, manual elevation corrections were applied to account for their elevated structure, thereby mitigating biases associated with incorrect flood detection. After that, road closures were implemented when the flood depth on the street exceeded 0.3 m, the permissible threshold for safe travel of vehicles[14,43]. Vehicles were dynamically rerouted based on the spatio-temporal closure of routes due to flood propagation, with rerouted vehicles taking alternative paths to reach their destinations. The travel time loss and emission measures were compared with the baseline traffic scenario to measure the indirect damage (user cost). In the microsimulation model, total trip-making demand was held constant across all scenarios, with trips canceled only when either the origin or the destination zone was directly inundated. Consequently, these trips were excluded from travel time and user cost calculations, reflecting the practical impossibility of initiating trips under inundated conditions. The user cost for each ward was calculated based on the proportion of each trip's travel time occurring within the ward, rather than being solely associated with the trip's origin or destination.

### Expected annual cost analysis

The expected annual cost (EAC) for isolated events-coastal, fluvial, and pluvial floods-was calculated by multiplying the damage associated with each event by their respective occurrence probabilities for baseline, 50-year, and 100-year return periods (Eq. (5)).

For compound flood events, we estimated the EAC by first determining the joint probability distribution of extreme rainfall, tidal surges, and river discharge using a trivariate Gumble copula[79–81] (Eq. (6)). This copula effectively captures the dependencies between the three variables, providing a robust framework for joint probability estimation.

$$\begin{aligned} \mathrm{EAC}_{(i)} = {} & P_{\mathrm{baseline}(i)} \times C_{\mathrm{baseline}(i)} \\ & + P_{50\mathrm{yr}(i)} \times C_{50\mathrm{yr}(i)} \quad i \in \{\mathrm{Coastal},\ \mathrm{Fluvial},\ \mathrm{Pluvial}\} \\ & + P_{100\mathrm{yr}(i)} \times C_{100\mathrm{yr}(i)} \end{aligned} \tag{5}$$

Where $\mathrm{EAC}_{(i)}$ represents the expected annual cost for coastal (C), fluvial (F), and pluvial (P) flooding events. The variable $P_{\mathrm{baseline}(i)}$ represents the probability of a baseline flood event occurring, while $C_{\mathrm{baseline}(i)}$ corresponds to the cost associated with the baseline flood event for the specific type of flood event $i$, where $i$ is Coastal, Fluvial, or Pluvial. Similarly, $P_{50\mathrm{yr}(i)}$ and $C_{50\mathrm{yr}(i)}$ represent the probability and associated cost for a 50-year flood event, and $P_{100\mathrm{yr}(i)}$ and $C_{100\mathrm{yr}(i)}$ are the probability and associated cost for a 100-year flood event.

The Gumbel copula for the three types of flooding can be expressed as:

$$\begin{aligned} C_\theta(u_{\mathrm{coastal}}, u_{\mathrm{fluvial}}, u_{\mathrm{pluvial}}) = {} & \Big[\big(-\ln(u_{\mathrm{coastal}})\big)^\theta + \big(-\ln(u_{\mathrm{fluvial}})\big)^\theta \\ & + \Big(-\ln(u_{\mathrm{pluvial}})\Big)^\theta\Big]^{\frac{1}{\theta}} \end{aligned} \tag{6}$$

Where The uniform random variables $u_{\mathrm{coastal}}$, $u_{\mathrm{fluvial}}$, $u_{\mathrm{pluvial}}$ represent the marginal distributions of the coastal, fluvial, and pluvial floods, respectively. The parameter $\theta$ is known as the dependence parameter of the Gumbel copula, and it indicates the strength of upper-tail dependence between these flooding events. A higher value of $\theta$ signifies a stronger dependence between extreme flood events in coastal, fluvial, and pluvial areas. The copula function $C_\theta(u_{\mathrm{coastal}}, u_{\mathrm{fluvial}}, u_{\mathrm{pluvial}})$ is used to capture the joint dependence structure among the coastal, fluvial, and pluvial flood events, thus modeling their combined risks.

The resultant probabilities for the baseline, 50-year, and 100-year scenarios were multiplied by the corresponding compound flood damages to estimate the Expected Annual Cost (EAC) for the compound flood event (Eq. (5). This EAC takes into account the dependence between the three flooding types, namely coastal, fluvial, and pluvial floods.

The EAC is further categorized into direct damage (agency cost) and indirect damage (user cost) for all scenarios, including both isolated and compound events. These damages are quantified in monetary terms. Additionally, the EAC related to vehicular emissions is expressed in tonnes. The GHG emissions are further broken down into specific components, including $CO_2$, CO, $PM_x$, and $NO_x$, providing a detailed assessment of the environmental impact associated with flood events.

## Data availability

The datasets used in this study are obtained from a combination of open repositories, institutional portals, and municipal records. Hourly precipitation data (0.1°) were retrieved from ERA5-Land via the Copernicus Climate Data Store (https://cds.climate.copernicus.eu/). Daily streamflow records for the Kuniyil station were accessed through the INDIWRIS portal (https://indiawris.gov.in/wris/#/). Hourly evapotranspiration data (0.25°) were obtained from the GLEAM dataset (https://www.gleam.eu/). Sub-hourly tide-level data were provided by INCOIS and are available upon request (https://incois.gov.in/portal/datainfo/drform.jsp). Digital elevation data includes inland topography from CartoDEM (NRSC) (https://www.nrsc.gov.in/nrscnew/Dataproducts_Thematic_cartodem.php) and coastal bathymetry from the NCEI Coastal DEM (NOAA) (https://www.ncei.noaa.gov/products/coastal-elevation-models). River cross-section data were collected through field surveys using ADCP and RTK methods. Stormwater drainage layout data, including manholes, pipes, and outfalls with capacity

attributes, were provided by the Kozhikode Municipal Corporation. Road network data were extracted from OpenStreetMap (OSM) (https://www.openstreetmap.com). Further details of all datasets are provided in Table S1.

## Code availability

The codes for this study are available at https://github.com/raviraj-dave96/Compoundflood_road_damage.

Received: 14 May 2025; Accepted: 22 October 2025;
Published online: 27 November 2025

## References

1. Vousdoukas, M. I. et al. Global probabilistic projections of extreme sea levels show intensification of coastal flood hazard. *Nat. Commun.* **9**, 2360 (2018).
2. Alfieri, L. et al. Global projections of river flood risk in a warmer world. *Earth's Future* **5**, 171–182 (2017).
3. CRED. Em-dat report 2023. Tech. Rep., Centre for Research on the Epidemiology of Disasters (CRED) (2023). https://files.emdat.be/reports/2023_EMDAT_report.pdf. Accessed: 2024-12-23.
4. Zhang, Y. J. et al. Simulating compound flooding events in a hurricane. *Ocean Dyn.* **70**, 621–640 (2020).
5. Maymandi, N., Hummel, M. A. & Zhang, Y. Compound coastal, fluvial, and pluvial flooding during historical hurricane events in the Sabine–Neches estuary, Texas. *Water Resour. Res.* **58**, e2022WR033144 (2022).
6. Du, H., Fei, K. & Gao, L. Nonlinear tide-river-surge interactions and their impacts on compound flooding during typhoon hato in the pearl river delta. *J. Geophys. Res.: Oceans* **129**, e2023JC020673 (2024).
7. Chan, F. K. S. et al. Building resilience in asian mega-deltas. *Nature Rev Earth & Env.* **5**, 522–537 (2024).
8. Bevacqua, E. et al. More meteorological events that drive compound coastal flooding are projected under climate change. *Commun. Earth Environ.* **1**, 47 (2020).
9. Gori, A. & Lin, N. Projecting compound flood hazard under climate change with physical models and joint probability methods. *Earth's Future* **10**, e2022EF003097 (2022).
10. Wahl, T., Jain, S., Bender, J., Meyers, S. D. & Luther, M. E. Increasing risk of compound flooding from storm surge and rainfall for major us cities. *Nat. Clim. Change* **5**, 1093–1097 (2015).
11. Martello, M. V. & Whittle, A. J. Estimating coastal flood damage costs to transit infrastructure under future sea level rise. *Commun. Earth Environ.* **4**, 137 (2023).
12. Tran, V. N. et al. Connectivity in urbanscapes can cause unintended flood impacts from stormwater systems. *Nat. Cities* **1**, 654–664 (2024).
13. Samadi, A., Jafarzadegan, K. & Moradkhani, H. Dem-based pluvial flood inundation modeling at a metropolitan scale. *Environ. Model. Softw.* **183**, 106226 (2025).
14. Pregnolato, M., Ford, A., Wilkinson, S. M. & Dawson, R. J. The impact of flooding on road transport: A depth-disruption function. *Transp. Res. D: Transp. Environ.* **55**, 67–81 (2017).
15. Yu, D. et al. Disruption of emergency response to vulnerable populations during floods. *Nat. Sustain.* **3**, 728–736 (2020).
16. Rajput, A. A., Nayak, S., Dong, S. & Mostafavi, A. Anatomy of perturbed traffic networks during urban flooding. *Sustain. Cities Soc.* **97**, 104693 (2023).
17. Rajput, A. A., Liu, C., Liu, Z. & Mostafavi, A. Human-centric characterization of life activity flood exposure shifts focus from places to people. *Nat. Cities* **1**, 264–274 (2024).
18. Pregnolato, M. et al. Assessing flooding impact to riverine bridges: An integrated analysis. *Nat. Hazards Earth Syst. Sci. Discuss.* **2020**, 1–18 (2020).
19. Papilloud, T., Röthlisberger, V., Loreti, S. & Keiler, M. Flood exposure analysis of road infrastructure–comparison of different methods at national level. *Int. J. Disaster Risk Reduct.* **47**, 101548 (2020).
20. Zhou, Y., Liu, K. & Wang, M. River flood risk assessment for the Chinese road network. *Transp. Res. part D: Transp. Environ.* **121**, 103818 (2023).
21. Yuan, H. et al. Matrix scenario-based urban flooding damage prediction via a convolutional neural network. *J. Environ. Manag.* **349**, 119470 (2024).
22. Kasmalkar, I. G. et al. When floods hit the road: Resilience to flood-related traffic disruption in the San Francisco Bay Area and beyond. *Sci. Adv.* **6**, eaba2423 (2020).
23. Pyatkova, K., Chen, A. S., Butler, D., Vojinović, Z. & Djordjević, S. Assessing the knock-on effects of flooding on road transportation. *J. Environ. Manag.* **244**, 48–60 (2019).
24. Li, Z., Yan, W. & Wang, L. Measuring mobility resilience with network-based simulations of flow dynamics under extreme events. *Transp. Res. Part D: Transp. Environ.* **135**, 104362 (2024).
25. Gori, A., Lin, N. & Xi, D. Tropical cyclone compound flood hazard assessment: From investigating drivers to quantifying extreme water levels. *Earth's Future* **8**, e2020EF001660 (2020).
26. Huang, W. et al. Compounding factors for extreme flooding around Galveston Bay during Hurricane Harvey. *Ocean Model.* **158**, 101735 (2021).
27. Sanders, B. F. et al. Large and inequitable flood risks in Los Angeles, California. *Nat. Sustain.* **6**, 47–57 (2023).
28. Ghosh, M., Mohanty, M. P., Kishore, P. & Karmakar, S. Performance evaluation of potential inland flood management options through a three-way linked hydrodynamic modelling framework for a coastal urban watershed. *Hydrol. Res.* **52**, 61–77 (2021).
29. Tanim, A. H., McKinnie, F. W. & Goharian, E. Coastal compound flood simulation through coupled multidimensional modeling framework. *J. Hydrol.* **630**, 130691 (2024).
30. Mühlhofer, E., Bresch, D. N. & Koks, E. E. Infrastructure failure cascades quintuple risk of storm and flood-induced service disruptions across the globe. *One Earth* **7**, 714–729 (2024).
31. Mei, C. et al. Analyzing urban form influence on pluvial flooding via numerical experiments using random slices of actual city data. *J. Hydrol.* **633**, 130916 (2024).
32. Dave, R., Subramanian, S. S. & Bhatia, U. Extreme precipitation induced concurrent events trigger prolonged disruptions in regional road networks. *Environ. Res. Lett.* **16**, 104050 (2021).
33. Arrighi, C., Pregnolato, M. & Castelli, F. Indirect flood impacts and cascade risk across interdependent linear infrastructures. *Nat. Hazards Earth Syst. Sci.* **21**, 1955–1969 (2021).
34. He, Y., Thies, S., Avner, P. & Rentschler, J. Flood impacts on urban transit and accessibility-a case study of kinshasa. *Transp. Res. part D: Transp. Environ.* **96**, 102889 (2021).
35. Dong, S., Gao, X., Mostafavi, A. & Gao, J. Modest flooding can trigger catastrophic road network collapse due to compound failure. *Commun. Earth Environ.* **3**, 38 (2022).
36. Hamedmoghadam, H., Jalili, M., Vu, H. L. & Stone, L. Percolation of heterogeneous flows uncovers the bottlenecks of infrastructure networks. *Nat. Commun.* **12**, 1254 (2021).
37. State Relief Commissioner, D. M. Kerala floods - 2018. Tech. Rep., State Disaster Management Authority, Kerala (2018).
38. Jayasimha Reddy, N. V. & Arunkumar, R. Development of flood inundation maps for the Chaliyar basin, Kerala under climate change scenarios. *Water Pract. Technol.* **18**, 2372–2383 (2023).
39. Achu, A., Gopinath, G. & Surendran, U. Machine learning framework for flood susceptibility modeling in a fast-growing urban city of southern India. In *International Conference on Hydraulics, Water Resources and Coastal Engineering*, 535–543 (Springer, 2021).
40. DHI. Mike+ by dhi (2023). https://www.dhigroup.com/technologies/mikepoweredbydhi/mikeplus. Accessed: 2025-01-18.
41. Lopez, P. A. et al. Microscopic traffic simulation using sumo. In *2018 21st international conference on intelligent transportation systems (ITSC)*, 2575–2582 (IEEE, 2018).

42. Google. Google Maps traffic data (2025). https://www.google.com/maps. Accessed: 2025-01-24.
43. Martinez-Gomariz, E., Gomez, M., Russo, B. & Djordjević, S. A new experiments-based methodology to define the stability threshold for any vehicle exposed to flooding. *Urban Water J.* **14**, 930–939 (2017).
44. Bates, P. D. et al. Combined modeling of us fluvial, pluvial, and coastal flood hazard under current and future climates. *Water Resour. Res.* **57**, e2020WR028673 (2021).
45. Xu, K., Zhuang, Y., Bin, L., Wang, C. & Tian, F. Impact assessment of climate change on compound flooding in a coastal city. *J. Hydrol.* **617**, 129166 (2023).
46. Wang, Z. et al. Compound coastal flooding in San Francisco Bay under climate change. *npj Nat. Hazards* **2**, 3 (2025).
47. Project, C. Augmented stereo strip triangulation (asst) software analysis & architecture document-sac/resipa/sipg/cartodem/tn-01/february. Tech. Rep., Space Application Centre (ISRO), Ahmedabad, India (2008).
48. Institute of Transportation Engineers. *Trip Generation Manual, Volume 2: Data* (Institute of Transportation Engineers, Washington, D.C., 2021), 11th edn.
49. Currans, K. M. & Clifton, K. J. Exploring ITE's trip generation manual: Assessing age of data and land-use taxonomy in vehicle trip generation for transportation impact analyses. *Transp. Res. Part A: Policy Pract.* **118**, 387–398 (2018).
50. Mukherjee, J. & Kadali, B. R. A comprehensive review of trip generation models based on land use characteristics. *Transp. Res. D: Transp. Environ.* **109**, 103340 (2022).
51. Department of Town and Country Planning, Government of Kerala. Kozhikode Master Plan for Land Use 2035 (2018). https://townplanning.kerala.gov.in/wp-content/uploads/2018/12/Kozhikode-plu-2035.pdf. Accessed: February 3, 2025.
52. Patgiri, U., Das Gupta, P. & Kanitkar, A. Mobility as a response to urban floods and its implications for risk mitigation: A local area level case study from Guwahati, Assam. In *Climate Crisis, Social Responses and Sustainability: Socio-ecological Study on Global Perspectives*, 487–520 (Springer, 2024).
53. Nithin, K., Mulangi, R. H. & Kumar, A. Travel decisions and experiences of bus passengers during extreme rainfall. *Technol. Sustain. Transp. Infrastruct.: Sel. Proc. SIIOC 2023* **529**, 297 (2024).
54. Huang, J. & Wang, J. Travel behavior resilience: Theory, method, and empirical studies. *J. Geog. Sci.* **34**, 1657–1674 (2024).
55. Aerts, J. C. et al. Evaluating flood resilience strategies for coastal megacities. *Science* **344**, 473–475 (2014).
56. DHI, M. F. 1d-2d modelling-user manual. *DHI Water & Environment, Hørsholm, Denmark* (2017).
57. for Environmental Information (NCEI), N. C. Coastal elevation models (2023). https://www.ncei.noaa.gov/products/coastal-elevation-models. Accessed: 2025-01-10.
58. NOAA Ocean Exploration. Acoustic Doppler Current Profiler (2023). https://oceanexplorer.noaa.gov/technology/acoust-doppler/acoust-doppler.html. Accessed: 2025-01-18.
59. Nakao, L. T. H., Krueger, C. P. & Bleninger, T. Benchmarking for using an acoustic doppler current profiler for bathymetric survey. *Environ. Monit. Assess.* **193**, 356 (2021).
60. Muñoz-Sabater, J. et al. Era5-land: A state-of-the-art global reanalysis dataset for land applications. *Earth Syst. Sci. Data* **13**, 4349–4383 (2021).
61. Hu, C. et al. Parameter regionalization with donor catchment clustering improves urban flood modeling in ungauged urban catchments. *Water Resour. Res.* **60**, e2023WR035071 (2024).
62. Chiew, F. H. et al. Application and testing of the simple rainfall-runoff model simhyd. In *Mathematical models of small watershed hydrology and applications.* pp. 335–367 (2002).
63. Bhasme, P. & Bhatia, U. Improving the interpretability and predictive power of hydrological models: Applications for daily streamflow in managed and unmanaged catchments. *J. Hydrol.* **628**, 130421 (2024).
64. Miralles, D. G. et al. Global land-surface evaporation estimated from satellite-based observations. *Hydrol. Earth Syst. Sci.* **15**, 453–469 (2011).
65. Satyanarayana, P. & Sharma, J. Web-enabled water resources information system of India (India-WRIS WebGIS) .
66. For Ocean Information Services (INCOIS), I. N. C. Tide gauge data (2023). https://incois.gov.in/portal/datainfo/tidegauge.jsp. Accessed: 2025-01-10.
67. (KSEOC), K. S. E. O. C. & (KSDMA), K. S. D. M. A. Flood affected 2018 - Kozhikode Corporation (2019). https://dmp.kila.ac.in/maps/Kozhikode/156-Kozhikkode_CORP/Flood%20affected%202018-126_Kozhikkode_Kozhikkode_Corp.pdf. Accessed: January 27, 2025.
68. (KSDMA), K. S. D. M. A. Kerala state disaster management authority (2023). https://sdma.kerala.gov.in/. Accessed: 2025-01-10.
69. OpenStreetMap contributors. Openstreetmap (2023). https://www.openstreetmap.org/. Accessed: 2025-01-10.
70. Huizinga, J., De Moel, H. & Szewczyk, W. Global flood depth-damage functions: Methodology and the database with guidelines. Tech. Rep., Joint Research Centre (2017).
71. World Bank. Consumer price index (CPI) (2023). https://data.worldbank.org/indicator/FP.CPI.TOTL. Accessed: 2025-01-10.
72. Krajzewicz, D., Erdmann, J., Behrisch, M. & Bieker, L. Recent development and applications of sumo-simulation of urban mobility. *Int. J. Adv. Syst. Meas.* (2012).
73. Contributors, O. W. Osm default maxspeed values for India. OpenStreetMap Wiki (2025). https://wiki.openstreetmap.org/wiki/OSM_tags_for_routing/Maxspeed#India. Default speed limits for various road types in India when 'maxspeed=*' is not tagged.
74. Chandra, S. & Kumar, U. Effect of lane width on capacity under mixed traffic conditions in India. *J. Transp. Eng.* **129**, 155–160 (2003).
75. Dhamaniya, A. & Chandra, S. Speed characteristics of mixed traffic flow on urban arterials. *Int. J. Civ., Environ., Struct., Constr. Archit. Eng.* **7**, 883–888 (2013).
76. Janson, B. N. Dynamic traffic assignment for urban road networks. *Transp. Res. Part B: Methodol.* **25**, 143–161 (1991).
77. Athira, I., Muneera, C., Krishnamurthy, K. & Anjaneyulu, M. Estimation of value of travel time for work trips. *Transp. Res. Procedia* **17**, 116–123 (2016).
78. Consortium, H. Handbook of emission factors for road transport (HBefa) (2025). https://www.hbefa.net/. Accessed: 2025-01-29.
79. Zellou, B. & Rahali, H. Assessment of the joint impact of extreme rainfall and storm surge on the risk of flooding in a coastal area. *J. Hydrol.* **569**, 647–665 (2019).
80. Xiao, H., Zhang, J. & Fang, H. A copula-based framework for joint encounter and state evolution analysis of urban short-duration rainstorm characteristics. *J. Hydrol.* **631**, 130823 (2024).
81. Khajehali, M., Safavi, H. R., Nikoo, M. R., Najafi, M. R. & Alizadeh-Sh, R. A copula-based multivariate flood frequency analysis under climate change effects. *Sci. Rep.* **15**, 146 (2025).


## Acknowledgements

The authors acknowledge the support of AICOE in Sustainable Cities Phase I/II, the ANRF (SERB) CRG grant (awarded to Udit Bhatia) #CRG/2023/001438, and the DST-NWO joint collaborative Water4Change program. Additionally, they express gratitude to CWRDM for providing the cartoDEM data and assisting with the field survey in Kozhikode. The authors also thank the members of the Machine Intelligence and Resilience Laboratory at IIT Gandhinagar for their valuable discussions and constructive feedback on this manuscript.

## Author contributions

R.D., U.B., S.S. and A.M. designed the experiments, R.D. performed the analysis, and R.D. and U.B. wrote the manuscript with input from S.S. and A.M.

## Competing interests

The authors declare no competing interests.

## Additional information

**Supplementary information** The online version contains supplementary material available at https://doi.org/10.1038/s42949-025-00288-8.

**Correspondence** and requests for materials should be addressed to Udit Bhatia.